^{96}Zr(n,γ) measurement at the n_TOF facility at CERN

G. Tagliente,[1,*] P. M. Milazzo,[2] K. Fujii,[2] U. Abbondanno,[2] G. Aerts,[3] H. Álvarez,[4] F. Alvarez-Velarde,[5] S. Andriamonje,[3] J. Andrzejewski,[6] L. Audouin,[7] G. Badurek,[8] P. Baumann,[9] F. Bečvář,[10] F. Belloni,[2] E. Berthoumieux,[3] F. Calviño,[11] M. Calviani,[12] D. Cano-Ott,[5] R. Capote,[13,14] C. Carrapiço,[15] P. Cennini,[16] V. Chepel,[17] E. Chiaveri,[16] N. Colonna,[1] G. Cortes,[11] A. Couture,[18] M. Dahlfors,[16] S. David,[9] I. Dillmann,[7,19] C. Domingo-Pardo,[20,19] W. Dridi,[3] I. Duran,[4] C. Eleftheriadis,[21] M. Embid-Segura,[5] A. Ferrari,[16] R. Ferreira-Marques,[17] W. Furman,[22] I. Goncalves,[15] E. Gonzalez-Romero,[5] F. Gramegna,[12] C. Guerrero,[5] F. Gunsing,[3] B. Haas,[23] R. Haight,[24] M. Heil,[7,19] A. Herrera-Martinez,[16] E. Jericha,[8] F. Käppeler,[7] Y. Kadi,[16] D. Karadimos,[25] D. Karamanis,[25] M. Kerveno,[9] E. Kossionides,[26] M. Krtička,[10] C. Lamboudis,[21] H. Leeb,[8] A. Lindote,[17] I. Lopes,[17] S. Lukic,[9] J. Marganiec,[6,19] S. Marrone,[1] T. Martínez,[5] C. Massimi,[27] P. Mastinu,[12] A. Mengoni,[13] C. Moreau,[2] M. Mosconi,[7,28] F. Neves,[17] H. Oberhummer,[8] S. O'Brien,[18] J. Pancin,[3] C. Papachristodoulou,[25] C. Papadopoulos,[29] C. Paradela,[4] N. Patronis,[25] A. Pavlik,[30] P. Pavlopoulos,[31] L. Perrot,[3] M. T. Pigni,[8] R. Plag,[7,19] A. Plompen,[32] A. Plukis,[3] A. Poch,[11] J. Praena,[12] C. Pretel,[11] J. Quesada,[14] R. Reifarth,[24,19] M. Rosetti,[33] C. Rubbia,[34] G. Rudolf,[9] P. Rullhusen,[32] J. Salgado,[15] C. Santos,[15] L. Sarchiapone,[16] I. Savvidis,[21] C. Stephan,[35] J. L. Tain,[20] L. Tassan-Got,[35] L. Tavora,[15] R. Terlizzi,[1] G. Vannini,[27] P. Vaz,[15] A. Ventura,[33] D. Villamarin,[5] M. C. Vincente,[5] V. Vlachoudis,[16] R. Vlastou,[29] F. Voss,[7] S. Walter,[7] M. Wiescher,[18] and K. Wisshak[7]

(n_TOF Collaboration)

[1]*Istituto Nazionale di Fisica Nucleare (INFN), Bari, Italy*
[2]*Istituto Nazionale di Fisica Nucleare (INFN), Trieste, Italy*
[3]*CEA, Irfu, Gif-sur-Yvette, France*
[4]*Universidade de Santiago de Compostela, Spain*
[5]*Centro de Investigaciones Energeticas Medioambientales y Technologicas, Madrid, Spain*
[6]*University of Lodz, Lodz, Poland*
[7]*Karlsruhe Institute of Technology (KIT), Campus Nord, Institut für Kernphysik, Karlsruhe, Germany*
[8]*Atominstitut der Österreichischen Universitäten,Technische Universität Wien, Austria*
[9]*Centre National de la Recherche Scientifique/IN2P3–IReS, Strasbourg, France*
[10]*Faculty of Mathematics and Physics, Charles University in Prague, Prague, Czech Republic*
[11]*Universitat Politecnica de Catalunya, Barcelona, Spain*
[12]*Istituto Nazionale di Fisica Nucleare (INFN), Laboratori Nazionali di Legnaro, Italy*
[13]*International Atomic Energy Agency (IAEA), NAPC/Nuclear Data Section, Vienna, Austria*
[14]*Universidad de Sevilla, Spain*
[15]*Instituto Tecnológico e Nuclear(ITN), Lisbon, Portugal*
[16]*CERN, Geneva, Switzerland*
[17]*LIP–Coimbra & Departamento de Fisica da Universidade de Coimbra, Portugal*
[18]*University of Notre Dame, Notre Dame, Indiana, USA*
[19]*GSI Darmstadt, Darmstadt, Germany*
[20]*Instituto de Física Corpuscular, CSIC–Universidad de Valencia, Spain*
[21]*Aristotle University of Thessaloniki, Greece*
[22]*Joint Institute for Nuclear Research, Frank Laboratory of Neutron Physics, Dubna, Russia*
[23]*Centre National de la Recherche Scientifique/IN2P3–CENBG, Bordeaux, France*
[24]*Los Alamos National Laboratory, Los Alamos, New Mexico, USA*
[25]*University of Ioannina, Greece*
[26]*NCSR, Athens, Greece*
[27]*Dipartimento di Fisica, Università di Bologna, and Sezione INFN di Bologna, Italy*
[28]*PTB Braunschweig, Braunschweig, Germany*
[29]*National Technical University of Athens, Greece*
[30]*University of Vienna, Faculty of Physics, Vienna, Austria*
[31]*Pôle Universitaire Léonard de Vinci, Paris La Défense, France*
[32]*CEC-JRC-IRMM, Geel, Belgium*
[33]*ENEA, Bologna, Italy*
[34]*Università degli Studi di Pavia, Pavia, Italy*
[35]*Centre National de la Recherche Scientifique/IN2P3–IPN, Orsay, France*

(Received 22 September 2011; published 14 November 2011)

The (n,γ) cross section of ^{96}Zr has been investigated at the CERN n_TOF spallation neutron source. High-resolution time-of-flight measurements using an enriched ZrO_2 sample allowed us to analyze 15 resonances below 40 keV with improved accuracy. On average, the capture widths were found to be 25% smaller than reported in earlier experiments. If complemented with the contribution by direct radiative capture, the derived

Maxwellian averaged cross sections are consistent with activation data at $kT = 25$ keV. The present results confirm the astrophysical implications for the s-process branching at ^{95}Zr.

DOI: 10.1103/PhysRevC.84.055802 PACS number(s): 25.40.Lw, 25.70.Ef, 27.60.+j, 26.20.Np

I. INTRODUCTION

The origin of the elemental abundances from iron to uranium can be almost completely assigned to neutron capture reactions in two main stellar scenarios, each being responsible for the production of about one half of the abundances in the mass region $A \geqslant 56$.

Explosive nucleosynthesis related to supernovae or neutron star mergers is characterized by complex reaction networks involving short-lived and very neutron rich nuclei. Because of the extremely high temperatures ($T > 10^9$ K) and neutron densities ($\gg 10^{20}$ cm^{-3}) the time scale for neutron capture is of the order of milliseconds. Accordingly, this process is known as the rapid neutron capture process or r-process [1].

The advanced burning phases of stellar evolution are series of neutron capture nucleosynthesis by slow neutron captures, the s-process. The s-process operates in thermally pulsing low-mass asymptotic giant branch (AGB) stars (main component, i.e., from Sr to Pb) [2] or during core He and shell C burning in massive stars (weak component, i.e., from Fe to Sr) [3]. During s-process conditions, temperatures are $\approx$(1–9) $\times 10^8$ K and neutron densities can vary between $\approx 10^6$ and 10^{13} cm^{-3}. Because typical neutron capture times are much larger than the average half-lives of β-unstable nuclei, the reaction path of the s-process follows the valley of stability by a sequence of neutron captures and β decays once an unstable isotope is encountered. Exceptions to this simple scheme occur at so-called branching points, unstable isotopes with half-lives comparable to the respective neutron capture time.

Situated at and near magic neutron number $N = 50$, the zirconium isotopes take a particular position on the s-process path, just at the border between the weak and main components, which dominate the s-abundances between Fe and Y on the one hand and from Zr up to the Pb/Bi region on the other hand. Because of their magic or near-magic neutron configurations all Zr isotopes exhibit relatively small (n,γ) cross sections and, in turn, comparably high s abundances. This holds especially for the neutron magic nucleus ^{90}Zr, but also for the stable isotopes ^{91}Zr, ^{92}Zr, and ^{94}Zr, which are all predominantly of s-process origin.

As far as the unstable isotopes ^{93}Zr and ^{95}Zr are concerned the first one can be considered as stable on the time scale of the s-process because of its long half-life of 1.5 Myr. The corresponding s abundance of ^{93}Zr decays only later to provide the s component of the daughter ^{93}Nb, which itself lies outside the s path. In contrast, ^{95}Zr represents a true branching point, where the reaction flow splits due to the competition between (n,γ) reactions and β decays. The comparably short half-life of ^{95}Zr ($t_{1/2} = 64$ d) prevents a large part of the reaction flow from reaching ^{96}Zr. Therefore, ^{96}Zr is traditionally considered as an r-process product with a small s-process admixture [4,5], given that it may be fed by the s-process only at neutron densities in excess of 3×10^8 cm^{-3}. To some extent, the s production of ^{96}Zr is favored, however, by its low neutron capture cross section, which, therefore, plays a key role in the analysis of the branching at $A = 95$.

In general, s-process branchings represent unique possibilities for constraining the physical conditions in the He burning zone near the stellar core [2,6,7]. The ^{95}Zr branching is sensitive to the conditions prevailing in thermally pulsing low-mass AGB stars, where ^{96}Zr is depleted between He shell flashes as a result of the low neutron density produced by the ^{13}C neutron source and replenished during the high neutron densities produced by ^{22}Ne(α, n) reactions during the He shell flashes. Thus, the s abundance for ^{96}Zr can be interpreted as an indicator for the efficiency of the ^{22}Ne neutron source.

Important constraints on nucleosynthesis can be obtained by the study of circumstellar dust grains recovered from meteorites [8]. In fact, the isotopic pattern of Zr observed in presolar grains [9] and particularly the relative abundances of ^{94}Zr and ^{96}Zr in silicon carbide (SiC) grains, which originate from AGB stars, provide information on the s-process efficiency in the parent stars.

Additional information derives from spectroscopic measurements on AGB stars, which are cool enough for ZrO to form in the atmosphere. The ^{94}Zr/^{96}Zr ratios obtained from analysis of the molecular bands indicate rather low ^{96}Zr abundances, although these stars exhibit clear s-process enhancements otherwise [10].

Precise knowledge of the ^{96}Zr(n,γ) cross section is mandatory for obtaining the ^{96}Zr/^{94}Zr ratio with the accuracy required for reliable analyses of ^{95}Zr branching. Moreover, it contributes also to an improved cross-section systematics and to the definition of the s-process path in a mass region where many cross-section data are still missing or uncertain [11,12].

Experimental data on resonance parameters in the energy range up to 40 keV have been reported in time-of-flight (TOF) measurements [13–16]. However, even the most recent data exhibit rather large uncertainties of 10 to 30% for the extracted capture kernels [14]. More accurate results have been reported from activation measurements in a quasistellar spectrum, which provided spectrum-averaged cross sections around 25 keV with uncertainties of 4.7 and 8.3% [17,18], much smaller than the discrepancies with respect to the TOF results.

In view of this situation an accurate measurement of the neutron capture cross section of ^{96}Zr has been carried out by the n_TOF Collaboration at CERN. The measurement and data analysis are described in Secs. II and III. Section IV deals with the resonance analysis. The results and their implications for stellar nucleosynthesis are discussed in Sec. V.

*Corresponding author: giuseppe.tagliente@ba.infn.it

†www.cern.ch/ntof

II. EXPERIMENTAL SETUP

The measurement was performed at the CERN n_TOF facility [19,20], where neutrons are produced by spallation reactions in a massive lead block by a 20 GeV/c pulsed proton beam. With the high beam energy, which yields 300 neutrons per proton, and an intensity of 7×10^{12} protons per pulse, a neutron flux of 10^5 neutrons/cm^2/pulse is obtained at the sample position 185 m from the target. The fast spallation neutrons are moderated in the 5.8-cm-thick layer of cooling water around the lead target, resulting in a wide neutron spectrum from thermal up to 250 MeV with a nearly constant isolethargic flux [$\Phi(E) \propto 1/E$] between 1 eV and 1 MeV. Due to the pulse width of 6 ns the resolution in neutron energy is better than 0.2% in the range of the present measurement, i.e., below 40 keV.

The experimental area is connected with the spallation target by an evacuated beam line. Background from the target is suppressed by heavy concrete walls and a massive iron shielding 3.5 m in thickness. Charged particles are removed from the neutron beam by a 1.5-T sweeping magnet. The neutron beam is shaped by two collimators at 135 and 175 m distance from the target.

The neutron flux was accurately determined relative to the ^{235}U(n,f) cross section by means of a calibrated fission chamber from PTB Braunschweig [20]. During the measurement, the flux was recorded by a low-mass neutron monitor located 1.5 m upstream of the capture samples, consisting of a Mylar foil 1.5 μm in thickness with a layer of 200 μg/cm^2 of ^{6}Li. The ejectiles from the ^{6}Li(n,α)^{3}H reaction were recorded by four Si detectors surrounding the sample outside the neutron beam [21].

A pair of C_6D_6 liquid scintillator cells was used to detect the prompt γ-ray cascades following neutron capture events. The detectors were designed for accurate measurements of resonance-dominated (n,γ) cross sections [22]. Possible background sources were minimized by reducing the detector mass to a thin carbon fiber cell, which is directly glued onto an EMI-9823QKB photomultiplier tube. The main constituents of the scintillator and of the detector, i.e., deuterium, C, O, and Si, were chosen for their very small (n,γ) cross sections. For the same reason, the sample changer was made from carbon fiber as well. The low neutron sensitivity obtained in this way is important in view of the large scattering-to-capture cross section ratio of ^{96}Zr.

The detectors were mounted perpendicular to the neutron beam at a distance of about 3 cm from the axis. Background due to in-beam γ rays, produced by neutron capture in the spallation target and predominantly in the water moderator, was reduced by placing the detectors 9.2 cm upstream of the sample position.

The light output of the detectors was calibrated at 662, 1173, and 1332 keV with ^{137}Cs and ^{60}Co reference sources. An additional calibration point at 6.13 MeV was obtained by means of a composite ^{238}Pu/^{13}C source. The calibrations were repeated in regular intervals to verify the stability of the detectors and of the data acquisition system.

The data acquisition system was based on fast digitizers operating at 500 MS million samples/s, corresponding to time steps of 2 ns. Each neutron burst could be registered for 16 ms by means of the 8-MB on-board memory of the digitizers. The signals were stored for off-line analysis of the deposited γ-ray energy and the respective TOF [23]. The TOF information was converted to neutron energy by means of the calibration described in Ref. [24].

TABLE I. Characteristics of the ^{96}Zr sample.

	Chemical form	Isotopic composition (%)				
		^{90}Zr	^{91}Zr	^{92}Zr	^{94}Zr	^{96}Zr
^{96}Zr	ZrO_2	19.41	5.21	8.20	8.68	58.5

The ^{96}Zr sample was prepared from ZrO_2 powder with an enrichment of 58.5%. The powder was pressed to a pellet 22 mm in diameter, 1.3 mm in thickness, and 3.398 g in mass. The pellet was canned in an aluminum capsule with 0.1-mm-thick walls and a mass of about 300 mg. The sample contained impurities of Hf, Sn, Na, Mg, and Al. Although the impurities contributed less than 0.01% to the total weight, various of the observed resonances in the TOF spectra had to be assigned to other Zr isotopes and to the impurities, in particular to Hf and Sn. This background contribution was carefully taken into account in data analysis.

In addition to ^{96}Zr, Au and Pb samples were used for monitoring the neutron flux and for background determination. All samples were 22 mm in diameter. The composition of the Zr sample is summarized in Table I.

III. DETERMINATION OF CAPTURE YIELDS

The neutron capture yield, which is defined as the fraction of incident neutrons undergoing (n,γ) reactions in the sample, is the experimental quantity for the resonance analysis described in Sec. IV.

Neutron capture reactions are characterized by the prompt γ-ray cascade emitted from the compound nucleus. In order to detect capture events independently of the cascade multiplicity, the intrinsic efficiency of C_6D_6 detectors has to be corrected by the pulse height weighting technique (PHWT) [25–27]. The PHWT represents an *a posteriori* manipulation of the detector response to ensure that the detector efficiency increases linearly with γ-ray energy. Then, the efficiency for capture cascades becomes proportional to the total released γ energy. To obtain the required linearity with γ-ray energy, each detector signal is multiplied with a weighting function (WF), a parametrized polynomial function of E_γ. Provided that the weighting function is properly determined, it has been demonstrated by a detailed study of the possible systematic uncertainties that an accuracy of 2% can be achieved with the PHWT [27].

Given the low neutron capture cross section of ^{96}Zr, the characterization of all possible backgrounds is of primary importance for this measurement. Different background components were identified from capture of sample-scattered neutrons in the detectors or in surrounding materials, from capture events in the aluminum can of the Zr sample, from

the ambient background in the experimental area, and mainly from in-beam γ rays produced in the spallation target. The evaluation of these backgrounds has been discussed in detail elsewhere [28].

Finally, the measured yield has been normalized by means of the saturated resonance technique [29], using the 4.9-eV resonance of ^{197}Au in the TOF spectrum of the 0.1-mm-thick Au sample. This absolute yield is directly linked to the capture and total cross sections and has been subject to an $\mathcal{R}$-matrix analysis, using the SAMMY code in the Reich-Moore approximation [30], to extract the individual resonance parameters.

IV. RESONANCE ANALYSES

The analysis was restricted to the energy range below 40 keV because of the limited counting statistics of the capture data at higher energies. The observed resonances were classified according to the composition of the sample, given the isotopic impurities and the specified contaminants. Except for a proposed new resonance at 35.88 keV, 14 of the 15 identified ^{96}Zr resonances were already listed in Refs. [13,14]. However, a resonance at 870 eV reported in a transmission measurement [31] and in the compilation of Ref. [32] was not observed.

Corrections for the energy resolution of the neutron beam, for the Doppler broadening of resonance widths, for isotopic and chemical sample impurities, and for self-shielding and neutron multiple scattering are considered in the fits with the SAMMY code. The effect of potential scattering was calculated using a nuclear radius of 6.8 fm [32].

The capture kernel of a resonance

$$K = g\frac{\Gamma_n\Gamma_\gamma}{(\Gamma_n+\Gamma_\gamma)}$$

is defined by the neutron and capture widths, Γ_n and Γ_γ, and the statistical spin factor

$$g = \frac{(2J+1)}{(2I_n+1)(2I_{Zr}+1)},$$

which is determined by the resonance spin, J, the spin of the incident neutron, $I_n = 1/2$, and the spin of the target nucleus, $I_{Zr} = 0$.

For the resonances under study, the neutron width Γ_n is always much bigger than the radiative width Γ_γ (with the exception of the first resonance at 301 eV). Because the capture kernels are therefore not sensitive to Γ_n, the statistical spin factor and Γ_n were kept fixed in the SAMMY fits, using the values from previous Zr analyses [33–37] and from the transmission measurement of Ref. [13]. The deduced resonance energies E_R, radiative widths Γ_γ, and capture kernels K are listed in Table II together with the adopted $g\Gamma_n$ values.

Examples illustrating the quality of the SAMMY fits are shown in Fig. 1.

Particular interest resides in the first resonance at 301 eV, which was well studied in the past [13,14,38,39]. The capture kernel values for this resonance are compared in Table III.

TABLE II. Resonance parameters E_R, Γ_γ, and $g\Gamma_n$ and capture kernels K.

E_R[a] (eV)	Γ_γ (meV)	$g\Gamma_n$[b] (eV)	K[c] (meV)
301.285(2)	—	—	113.3(3)
3820.5(1)	35.(1)	3.93	35.(1)
4135.3(3)	54.(2)	14.9	106.(3)
5445.5(8)	58.(2)	25.3	58.(2)
5974.9(2)	92.(2)	11.6	181.(4)
9009(1)	47.(3)	9.9	47.(3)
13286.0(7)	40.(2)	6.0	79.(4)
15150.8(5)	174.(6)	9.2	336(11)
15432(11)	77.(9)	66.1	77.(9)
17790.9(9)	113.(5)	16.1	223(11)
24703(7)	35.(5)	13.6	35.(5)
29815(15)	341(24)	584.	681(50)
35186(18)	145(32)	67.3	144(30)
35880(19)	—	—	[149(24)]
36671(11)	102(23)	141.	203(46)

[a]The notation 301.285(2) for the uncertainties is equivalent to 301.285 ± 0.002.

[b]Except for the first resonance the values of $g\Gamma_n$ used in the SAMMY fit were adopted from Ref. [13].

[c]Uncertainties of K account only for the statistical part.

The present value is in good agreement with those from Coceva *et al.* [13] and Brusegan *et al.* [14] and with the one from Salah *et al.* [38], but it disagrees with the value of Leinweber *et al.* [39], indicating that the Γ_γ data obtained in that experiment are probably too low, as already noted in Ref. [32].

As a consequence of the relatively small neutron capture cross section of ^{96}Zr, the limited counting statistics contribute substantially to the overall experimental uncertainty. Because

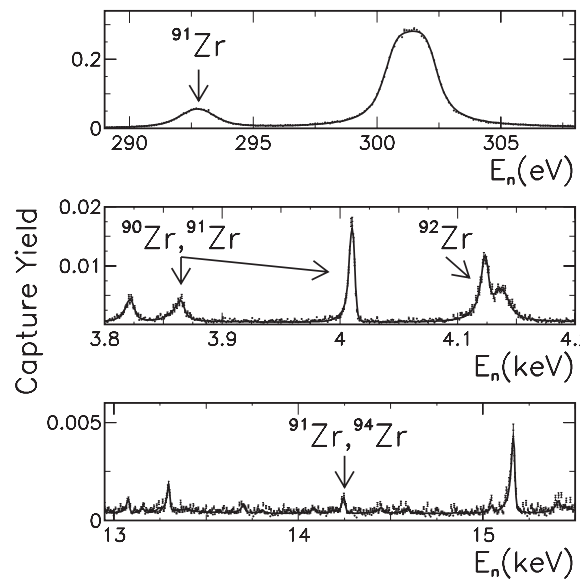

FIG. 1. Examples for fits of the capture yield with the $\mathcal{R}$-matrix code SAMMY. Isotopic and elemental impurities in the sample were included in the fit according to their abundances.

TABLE III. Capture kernels of the first resonance at 301 eV from different experiments.

Reference	Type of experiment	K (meV)
[13,14]	Transmission + Capture	117.3 ± 3.
[38]	Transmission	125.1 ± 8.
[39]	Transmission + Capture	87. ± 3.
This work	Capture	113.3 ± 3.

of the decreasing signal/background ratio, statistical uncertainties per resonance are increasing with neutron energy from ≈3% at 300 eV to ≈6% at 40 keV. Systematic uncertainties arise from the energy dependence of the neutron flux and from the fraction of the neutron beam covered by the sample. For the latter contributions an uncertainty of 2% was determined by means of the saturated resonance technique using the 4.9-eV resonance of ^{197}Au. The application of the PHWT adds another systematic uncertainty of 2%, as discussed in Ref. [27].

The present results can be compared with data from a measurement at the electron linear accelerator at IRMM Geel, which were obtained more than 30 years ago with fluorocarbon C_6F_6 scintillators [14]. These data represent the only complete set of resonance parameters in the energy range below 40 keV. On average, the present results for Γ_γ are 25% lower than the values given in Ref. [14], as illustrated in Fig. 2(a). Because $\Gamma_n \gg \Gamma_\gamma$ the same picture is observed in the comparison of the capture kernels in Fig. 2(b).

The likely reason for these systematic differences could be that the neutron sensitivity had been underestimated in Ref. [14]. In this respect, the low neutron-induced background obtained with the optimized experimental setup and with the extremely small duty factor of the n_TOF facility represents a substantial improvement in measurements of small capture cross sections as in the case of ^{96}Zr.

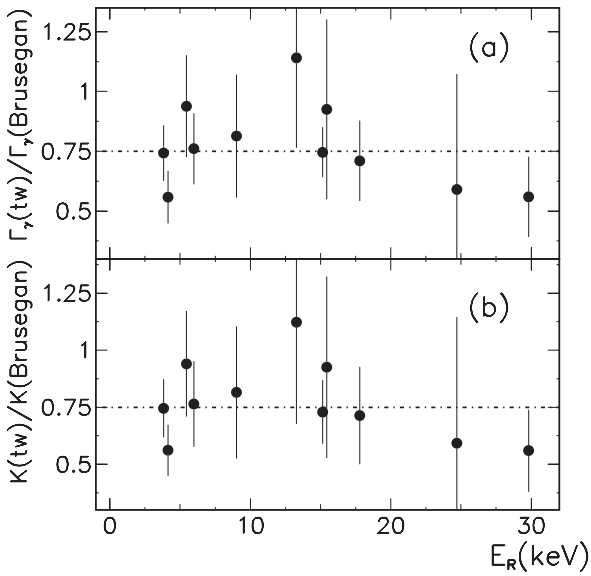

FIG. 2. Ratio between Γ_γ values (a) and capture kernels (b) obtained in this work (tw) and the results reported in Ref. [14]. The average ratios are indicated by dashed-dotted lines.

V. ASTROPHYSICAL IMPLICATIONS

A. Maxwellian average cross sections

The abundances produced in the s-process in thermally pulsing low-mass AGB stars can be quantitatively described provided that the stellar (n,γ) cross sections of the involved isotopes are reliably known. The respective Maxwellian averaged cross sections (MACS) [11] can be calculated by folding the experimental values for $\sigma(E_n)$ with the thermal stellar neutron spectra characteristic of the s-process site. The temperatures during the He-shell-burning episodes in AGB stars are 90 and 250 MK, corresponding to effective thermal energies of $kT = 8$ and 23 keV [48]. Accordingly, the energy-differential cross section is required in an energy range from about 300 eV to roughly 200 keV. (This range could extend up to 500 keV for the highest temperatures during shell C burning in massive stars, which is relevant for the mass region between Fe and Sr, but contributes only a minute fraction to the Zr abundances.)

In view of the restricted energy range covered in this work, the present experimental data have to be complemented for the neutron energy range above 40 keV. The evaluated data set from the very recently released JENDL-4.0 library [40] was chosen for that purpose.

The contribution of the present results to the MACS values is illustrated for different thermal energies in Fig. 3(a), which shows the fraction of the MACS that is obtained if the integration is limited to neutron energies below 40 keV relative to the total MACS. One finds that practically 100% of the MACS at $kT = 8$ keV is determined by the resonances

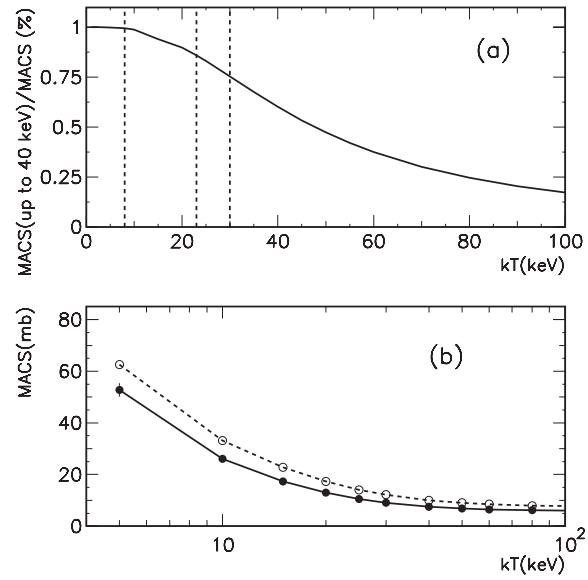

FIG. 3. (a) Ratio between MACS values calculated with an upper integration limit of 40 keV and the total MACS determined by complementing the present data with the evaluated cross section from the JENDL-4.0 library [40] (reduced to 78% to match the present results below 40 keV). The relevant thermal energies of 8, 23, and 30 keV are indicated by dashed lines. (b) MACS as a function of thermal energy. The present results (full circles) are systematically lower than the corresponding values calculated from the JENDL evaluation [40] (open circles).

TABLE IV. Comparison with MACS values at a thermal energy of 30 keV (using data from Ref. [12]).

MACS (mb)	Reference	Year
Theoretical calculations		
28	[41]	1976
58	[42]	1981
11	[43]	2000
3.2	[44]	2005
Evaluated values		
12.3	[40]	2005
10.3	[45]	2006
Experimental results		
41 ± 12	[15]	1967
30 ± 12	[16]	1971
12 ± 1	[18]	1983
10.7 ± 0.5[a]	[17]	1990
9.0 ± 0.6	This work	

[a]Recommended value in Ref. [12].

in the investigated energy range, and 85% are still covered at the higher thermal energy of $kT = 23$ keV reached during He shell flashes. At the thermal value of $kT = 30$ keV, which is traditionally used for the comparison of MACS results, this fraction is 75%.

The total MACS values were obtained by complementing the measured data above the present upper limit of 40 keV with the evaluated cross section from the JENDL-4.0 library [40], normalized by a factor of 0.78 to match the present results.

In Fig. 3(b) the MACS values obtained in that way are compared to the respective values if only the evaluated cross section in the JENDL library [40] had been used. The fact that the slope of the present data set confirms the energy dependence of the JENDL evaluation justifies the choice of this data library to complement our data above 40 keV.

The MACS values for a thermal energy of $kT = 30$ keV are summarized in Table IV. Apart from theoretical data [41–44], evaluated cross sections [40,45], and the rather uncertain data based on older experiments [15,16], the present result is distinctly smaller than the one obtained in the activation measurement of Ref. [17]. This difference may well be due to the contribution of the direct radiative capture (DRC) channel, which varies smoothly with neutron energy, and is, therefore, not covered by the resonance analysis.

The DRC component in the reaction process has been calculated using the two-body potential model with bound-state wave functions determined by a Woods-Saxon mean-field potential with fixed well-depth parameters to reproduce the experimental binding energy B_n (Table V).

With that model, the DRC cross section was obtained by determining the overlap integral of the bound-state wave functions with the continuum wave functions. The latter were derived from the scattering matrix elements (phase shifts) for a mean-field potential with the same geometrical parameters. The available values for the scattering length $a_{\rm coh} = 5.44 \pm 0.1$ [46] and 7.1 ± 0.2 fm [47] correspond to a range of mean-field potentials, V_0, which yield a DRC component compatible with the difference in the MACS data from the present TOF analysis and the activation measurement of Ref. [17]. Because its shape is well defined, we normalized the DRC component to reproduce the MACS of 11.6 ± 0.4 mb measured by activation and obtained a DRC contribution of 1.1 mb at $kT = 25$ keV. However, this approach was found to provide viable solutions only in the energy range below about 100 keV, i.e., for thermal energies below $kT = 25$ keV. At higher energies, the DRC results are becoming increasingly sensitive to the choice of V_0, which leads also to large uncertainties in the DRC contributions.

TABLE V. Wood-Saxon parameters used in the calculation of the bound-state and scattering wave functions.

Radius parameter $r_0 = 1.2360$ fm
Diffuseness $d = 0.62$ fm
Spin orbit strength $V_{so} = 7$ MeV

$n\ell j$	B_n (MeV)	J_f[a]	Well depth V_0 (MeV)
$3s1/2$	5.575	0.5	49.2
$2d3/2$	4.471	1.5	48.5
$1g7/2$	4.309	3.5	46.3

[a]Total spin of the final (bound) state.

This situation is reflected in Table VI, where the MACS values derived from the present resonance analysis (complemented by the evaluated cross sections above 40 keV from the JENDL-4.0 library) are listed together with the normalized DRC components. Above $kT = 25$ keV, the DRC values and the corresponding total MACS data are given in parentheses to indicate this uncertainty.

Fortunately, the correction works in the entire range of thermal energies of relevance for the *s*-process in low-mass AGB stars, which contribute the major *s* component of ^{96}Zr. In this temperature regime there is very good agreement with

TABLE VI. Comparison of MACS values at different thermal energies.

kT (keV)	MACS (mb)				
	This work	DRC[a]	Total	Ref. [40]	Ref. [12]
5	52.8 ± 2.6	0.3	53.1 ± 2.6	68.7	56
10	26.1 ± 1.3	0.5	26.6 ± 1.3	34.8	28
15	17.3 ± 0.9	0.7	18.0 ± 0.9	23.4	19
20	13.0 ± 0.7	0.9	13.9 ± 0.7	17.7	14
25	10.5 ± 0.6	1.1	11.6 ± 0.7	14.3	12
30	9.0 ± 0.6	(1.3)	(10.3)	12.3	10.7
40	7.5 ± 0.5	(1.7)	(9.2)	10.0	8.3
50	6.8 ± 0.5	(2.0)	(8.8)	9.0	6.8
60	6.4 ± 0.5	(2.1)	(8.5)	8.4	5.8
80	6.1 ± 0.5	(2.3)	(8.4)	7.8	4.4
100	6.0 ± 0.5	(2.2)	(8.2)	7.5	3.5

[a]DRC component normalized to fit the activation result from Ref. [17]. Values above $kT = 25$ keV are given in parentheses to indicate the uncertainty in the DRC calculation arising from the sensitivity on the potential strength used to calculate the scattering wave functions (continuum), mostly of *p*-wave character.

the recommended MACS data in the compilation of Ref. [12], as shown in Table VI. For thermal energies above 50 keV, however, the present data are increasingly larger than those in Ref. [12].

B. The *s*-process branching at ^{95}Zr

In general, the stellar production of ^{96}Zr in low-mass AGB stars as well as in massive stars is hampered because the half-life of ^{95}Zr ($t_{1/2} = 64$ d) is much shorter than the respective neutron capture times. Therefore, the reaction chain of the *s*-process is mostly determined by the β decay rate, and ^{96}Zr is fed only by a weak branch of the reaction flow.

The analysis of this branching is complicated for several reasons. From the *s*-process point of view, ^{96}Zr lies at the border between the weak and main *s* components, which are associated with massive stars and low-mass AGB stars, respectively. These sites are characterized by different temperature and neutron density regimes. While the weak component is not expected to contribute significantly to the abundance of ^{96}Zr [49,50], the main component depends critically on the strength of the ^{95}Zr branching.

The fact that the MACS for ^{96}Zr was confirmed by the present results implies that the destruction rate is well described in *s*-process calculations, in contrast with its rate for production via ^{95}Zr(n,γ) reactions. Because there are no experimental data to determine the MACS of ^{95}Zr, theoretical predictions with the Hauser-Feshbach (HF) statistical model have to be used. However, such predictions are uncertain in cases where the level density of the compound system is low, i.e., for neutron-rich isotopes and in the vicinity of magic neutron numbers. Because both criteria apply to ^{95}Zr, the recommended MACS in Ref. [12] is given with a semiempirical correction of the HF calculation.

Based on this value, the detailed *s*-process model for low-mass AGB stars used in Ref. [6] yields an *s* contribution of 55% for the observed ^{96}Zr abundance. This value turned out to be in sharp contrast to the isotopic abundance patterns of ZrO in the envelopes of cool AGB stars, which were observed via optical lines in molecular bands [10], as well as with the isotope ratios in presolar silicon carbide grains, which also show very small ^{96}Zr components [51,52]. This deficit in ^{96}Zr could be explained by recent nucleosynthesis studies of Travaglio *et al.* [53], who found that most of the ^{96}Zr could have been produced by the *p*-process in explosively burning Ne/O layers of type Ia supernovae.

With these indications, only a small fraction of ^{96}Zr can actually be attributed to the *s*-process. In turn, this means that the MACS of ^{95}Zr has presumably been overestimated in Ref. [12]. Therefore, a satisfactory analysis of the branching at $A = 95$ has to await the improvement of the ^{95}Zr(n,γ) cross section, possibly by an updated MACS systematics using recent cross sections for the stable Zr isotopes [33–37], or—on the long run—by a direct experimental determination of the ^{95}Zr cross section itself.

With respect to the branching problem, it should also be noted that the solar Zr abundance has recently been reduced by ≈6% [54] compared to a previous compilation [55] that had been used in earlier *s*-process studies [6].

VI. CONCLUSIONS

The (n,γ) cross section of ^{96}Zr has been measured with improved accuracy in the neutron energy range up to 40 keV by taking advantage of the unique features of the n_TOF facility at CERN. Resonance parameters were determined for 15 resonances. The capture kernels of these resonances were found to be significantly smaller than reported in previous TOF measurements. This might be the consequence of improvements concerning the experimental setup and the data analysis package. For thermal energies below $kT =$ 30 keV, the Maxwellian averaged cross sections calculated from the present data exhibit uncertainties of 5 to 7%, but they are smaller than obtained in activation measurements of comparable accuracy. This difference is ascribed to a contribution of the DRC channel, which is not included in the resonance analysis of TOF data measured with C_6D_6 scintillation detectors.

The present result provides important information for investigating the *s*-process branching at ^{95}Zr, because it yields the destruction rate of ^{96}Zr under neutron irradiation in the *s*-process. To resolve existing differences in observed Zr isotope ratios in cool giants and presolar SiC grains, reliable information is also needed for the production rate, i.e., the stellar (n,γ) cross section of the unstable branch point isotope ^{95}Zr.

ACKNOWLEDGMENTS

This work was supported by the EC under Contract No. FIKW-CT-2000-00107 and by the funding agencies of the participating institutes.

[1] E. M. Burbidge, G. R. Burbidge, W. A. Fowler, and F. Hoyle, Rev. Mod. Phys. **29**, 547 (1957).
[2] R. Gallino, C. Arlandini, M. Busso, M. Lugaro, C. Travaglio, O. Straniero, A. Chieffi, and M. Limongi, Astrophys. J. **497**, 388 (1998).
[3] C. M. Raiteri, M. Busso, R. Gallino, and G. Picchio, Astrophys. J. **371**, 665 (1991).
[4] A. G. W. Cameron, Space Sci. Rev. **15**, 121 (1973).
[5] F. Käppeler, Prog. Nucl. Part. Phys. **43**, 419 (1999).
[6] C. Arlandini, F. Käppeler, K. Wisshak, R. Gallino, M. Lugaro, M. Busso, and O. Straniero, Astrophys. J. **525**, 886 (1999).
[7] M. Lugaro, F. Herwig, J. C. Lattanzio, R. Gallino, and O. Straniero, Astrophys. J. **586**, 1305 (2003).
[8] E. Anders and E. Zinner, Meteoritics **28**, 490 (1993).
[9] M. Lugaro, A. M. Davis, R. Gallino, J. Pellin, O. Straniero, and F. Käppeler, Astrophys. J. **593**, 486 (2003).
[10] D. L. Lambert, V. V. Smith, M. Busso, R. Gallino, and O. Straniero, Astrophys. J. **450**, 302 (1995).
[11] Z. Y. Bao, H. Beer, F. Käppeler, F. Voss, K. Wisshak, and T. Rauscher, At. Data Nucl. Data Tables **76**, 70 (2000).
[12] I. Dillmann, M. Heil, F. Käppeler, R. Plag, T. Rauscher, and F.-K. Thielemann, in *Capture Gamma-Ray Spectroscopy and Related Topics*, AIP Conference Series 819, edited by A. Woehr

and A. Aprahamian (American Institute of Physics, New York, 2005), p. 123 (see also [http://www.kadonis.org]).
[13] C. Coceva, P. Giacobbe, and M. Magnani, in *Nuclear Cross Sections for Technology*, edited by J. L. Fowler, C. H. Johnson, and C. D. Bowman, (National Bureau of Standards, Washington DC, 1980), NBS Special Publication 594, p. 319.
[14] A. Brusegan, F. Corvi, G. Rohr, and B. J. Allen, in *Neutron-Capture Gamma-Ray Spectroscopy and Related Topics 1981*, edited by T. Von Egidy, F. Gönnenwein, B. Maier (Institute of Physics, Bristol, 1981), p. 406; data in the EXFOR nuclear data library are at [www-nds.iaea.org/exfor].
[15] R. Macklin and J. Gibbons, Phys. Rev. **159**, 1007 (1967).
[16] B. Allen, J. Gibbons, and R. Macklin, Adv. Nucl. Phys. **4**, 205 (1971).
[17] K. Toukan and F. Käppeler, Astrophys. J. **348**, 357 (1990).
[18] J. Wyrick and W. Poenitz, Technical Report ANL-83-4, Argonne National Laboratory, 1983, p. 196.
[19] U. Abbondanno *et al.*, CERN n_TOF facility: Performance Report, CERN-SL-2002-053 ECT, 2003.
[20] C. Borcea *et al.*, Nucl. Instrum. Methods A **513**, 523 (2003).
[21] S. Marrone *et al.*, Nucl. Instrum. Methods A **517**, 389 (2004).
[22] R. Plag, M. Heil, F. Käppeler, P. Pavlopoulos, R. Reifarth, and K. Wisshak, Nucl. Instrum. Methods A **496**, 425 (2003).
[23] U. Abbondanno *et al.*, Nucl. Instrum. Methods A **538**, 692 (2005).
[24] G. Lorusso *et al.*, Nucl. Instrum. Methods A **532**, 622 (2004).
[25] F. Corvi *et al.*, Nucl. Sci. Eng. **107**, 272 (1991).
[26] J. N. Wilson *et al.*, Nucl. Instrum. Methods A **511**, 388 (2003).
[27] U. Abbondanno *et al.*, Nucl. Instrum. Methods A **521**, 454 (2004).
[28] R. Terlizzi *et al.*, Phys. Rev. C **75**, 035807 (2007).
[29] R. L. Macklin and J. Halperin, Phys. Rev. C **14**, 1389 (1976).
[30] N. M. Larson, Updated Users' Guide for SAMMY: Multilevel *R*-matrix fits to neutron data using Bayes' equations, SAMMY computer code, Report No. ORNL/TM-9179/R7, Oak Ridge National Laboratory, 2006.
[31] A. R. de L. Musgrove, W. M. Good, and J. A. Harvey, Australian Atomic Energy Commission Report No. E415, 1977.
[32] S. F. Mughabghab, *Neutron Cross Sections: Neutron Resonances, Resonance Parameters and Thermal Cross Sections* $Z = 1$–100 (Elsevier Science, Amsterdam, 2006).
[33] G. Tagliente *et al.*, Phys. Rev. C **77**, 035802 (2008).
[34] G. Tagliente *et al.*, Phys. Rev. C **78**, 045804 (2008).
[35] G. Tagliente *et al.*, Phys. Rev. C **81**, 055801 (2010).
[36] G. Tagliente *et al.* (private communication).
[37] G. Tagliente *et al.*, Phys. Rev. C **84**, 015801 (2011).
[38] M. M. Salah *et al.*, Conf. on Nucl. Data for Basic and Appl. Sci., Santa Fé (USA) **1**, 593 (1985).
[39] G. Leinweber *et al.*, Nucl. Sci. Eng. **134**, 50 (2000).
[40] K. Shibata *et al.*, J. Nucl. Sci. Technol. **48**, 1 (2011).
[41] J. Holmes, S. Woosley, W. Fowler, and B. Zimmerman, At. Data Nucl. Data Tables **18**, 305 (1976).
[42] M. Harris, Astrophys. Space Sci. **77**, 357 (1981).
[43] T. Rauscher and F.-K. Thielemann, At. Data Nucl. Data Tables **75**, 1 (2000).
[44] S. Goriely, Hauser-Feshbach Reaction Rates for Nuclei with $Z = 8$–109 (version 8/29/2005), [http://www-astro.ulb.ac.be/Html/hfr.html].
[45] M. B. Chadwick *et al.*, Nucl. Data Sheets **107**, 2931 (2006).
[46] L. Koester, H. Rauch, and E. Seymann, Nucl. Data Sheets **49**, 65 (1991).
[47] S. F. Mughabghab, M. Divadeenam, and N. E. Holden, *Neutron Cross Sections* (Academic, New York, 1981), Vol. 1, Part A.
[48] R. Gallino, C. Arlandini, M. Busso, M. Lugaro, C. Travaglio, O. Straniero, A. Chieffi, and M. Limongi, Astrophys. J. **497**, 388 (1998).
[49] C. M. Raiteri, R. Gallino, M. Busso, D. Neuberger, and F. Käppeler, Astrophys. J. **419**, 207 (1993).
[50] M. Pignatari, R. Gallino, M. Heil, M. Wiescher, F. Käppeler, F. Herwig, and S. Bisterzo, Astrophys. J. **710**, 1557 (2010).
[51] E. Zinner, Annu. Rev. Earth Planet Sci. **26**, 147 (1998).
[52] G. K. Nicolussi *et al.*, Science **277**, 1281 (1997).
[53] C. Travaglio, F. K. Röpke, R. Gallino, and W. Hillebrandt (private communication).
[54] K. Lodders, H. Palme, and H.-P. Gail, *The Landolt-Börnstein Database, Vol. 4.4, Abundances of the Elements in the Solar System* (Springer, Berlin, 2009).
[55] E. Anders and N. Grevesse, Geochim. Cosmochim. Acta **57**, 197 (1989).